Size Effects in Cluster Infrared Spectra: the ν_1 Band of Ar_n-HCO^+ ($n = 1-13$)

S. A. Nizkorodov, O. Dopfer, T. Ruchti, M. Meuwly, J. P. Maier, and E. J. Bieske*,†

Institut für Physikalische Chemie, Universität Basel, Klingelbergstrasse 80, CH-4056 Switzerland

Received: July 12, 1995; In Final Form: September 12, 1995[⊗]

Spectroscopic and dynamical properties of the Ar_n-HCO^+ ($n = 1-13$) cluster series have been explored by exciting the chromophore HCO^+ in the vicinity of its ν_1 C−H stretch transition. Spectra were obtained by mass selecting the clusters, exposing them to tunable, pulsed IR light (0.02 cm^{-1} bandwidth), and monitoring the fragment intensity as a function of laser frequency. The ν_1 band of the $Ar-HCO^+$ dimer is rotationally resolved and has a form consistent with a linear proton-bound complex. Analysis in terms of a pseudodiatomic Hamiltonian yields the following parameters: $\nu_0 = 2815.063 \pm 0.020$ cm^{-1}, $B'' = 0.06646 \pm 0.000\,08$ cm^{-1}, $D'' = (7 \pm 4) \times 10^{-8}$ cm^{-1}, $B' = 0.06829 \pm 0.000\,08$ cm^{-1}, $D' = (17 \pm 4) \times 10^{-8}$ cm^{-1}. The rotational line widths indicate a lifetime of more than 250 ps for the optically prepared state. The ν_1 vibrational bands of the larger Ar_n-HCO^+ clusters, while lacking resolved rotational structure, are still reasonably narrow (<10 cm^{-1}) and decrease in width as the cluster size increases. Excitation of the ν_1 transition in Ar_n-HCO^+ ($n = 2-13$) results in the production of a relatively narrow range of daughter ions. Incremental Ar binding energies are extracted from the branching ratio data using a statistical model which takes into account the kinetic energy of the departing Ar atoms. The variation with cluster size of the binding energies, vibrational band shifts, and combination band spacings are argued to be evidence for Ar_n-HCO^+ structures where Ar atoms form primary and secondary solvation rings about a linear $Ar-HCO^+$ core with shell completion at $n = 12$. This view is consistent with simple empirical potential energy calculations.

I. Introduction

For several decades chemists and physicists have explored phenomena surrounding microsolvation in small heterogeneous gas phase clusters. Much of the work has been motivated by a desire to follow the development of aggregate properties as the size of cluster increases and to connect the properties of the isolated constituents with those of the bulk. Several general directions have been apparent in the experimental determination of aggregate structures. On the one hand have been mass spectrometry based experiments that have successfully followed the size dependence of neutral and ionic cluster properties, including ionization potentials, electron detachment energies, metastable fractions, reactivities, and collision-induced dissociation cross sections (see contributions to refs 1 and 2). While these experiments have seldom yielded direct structural information, aberrations in the development of a particular property with increasing cluster size have often been linked with arrangements having a satisfying regularity. For example, it has been observed that when clusters are composed mainly of atoms that interact more or less isotropically with one another (e.g., Ar_n^+ [3] or $O^-(Ar)_n$[4] clusters), certain sizes where monomer coordination is optimized are particularly abundant and that these correspond to the icosahedral structures first described by Mackay.[5]

Parallel to these experiments on ionic species have been elegant studies where structural attributes of smaller *neutral* clusters (e.g., Ar_n-HF and Ar_n-HCl, $n = 1-4$) have been inferred directly from spectroscopic measurements conducted in the microwave,[6] far-infrared,[7] and mid-infrared[8] regions. While these high-resolution spectroscopic approaches have revealed rather precise structural details, several factors including limited sensitivity, spectral congestion, and the fact that usually spectral analysis (not a trivial matter for larger floppy systems) necessarily precedes species identification have restricted these methods to rather small systems. In order to avoid some of these difficulties, an approach involving cluster size selection through scattering by a second molecular beam has been developed.[9−11] As well, there is a large body of experimental work where the properties of neutral complexes and clusters have been investigated by exciting *electronic* transitions. In this case, resonant multiphoton ionization coupled to time of flight mass spectrometry has often been used to help identify the absorbing cluster, although there are sometimes difficulties in the secure identification of the parent cluster due to post-ionization fragmentation.

The difficulties surrounding the selection of neutral clusters can be neatly circumvented if one concentrates instead on *ionic* species where mass spectrometry can be coupled with laser spectroscopy to probe the attributes of size selected ionic clusters.[12−15] Photoexcitation of discrete resonances embedded in the dissociative continuum can be inferred from the cluster's subsequent fragmentation to produce daughter ions of different mass. The main disadvantage of the approach is that photon absorption must eventually lead to dissociation in order for the transition to be inferred. Of singular significance have been the mid-infrared studies by these means of protonated clusters including $H_3^+-(H_2)_n$,[13] $H_3O^+-(H_2O)_n$,[14] and $NH_4^+-(NH_3)_n$.[15] In these cases, structural features have been inferred from the strength and disposition of vibrational bands associated with either the core or the ligands, a classic example being $NH_4^+-(NH_3)_n$, where identifiable vibrational bands have been associated with the first and subsequent coordination shells.[15,16]

The present paper describes an extension of this work towards the characterization of larger ionic complexes, with a mid-infrared spectroscopic investigation of *size-selected* Ar_n-HCO^+ ($n = 1-13$) clusters. As the proton affinity of CO (142 kcal/mol[17]) by far exceeds that of Ar (88.6 kcal/mol[17]), the Ar_n-HCO^+ clusters should be composed essentially of an HCO^+ core surrounded by perturbing Ar solvent atoms. Nevertheless, the intermolecular interactions should be strong and some

† Present address: School of Chemistry, The University of Melbourne, Parkville, Victoria 3052, Australia.

[⊗] Abstract published in *Advance ACS Abstracts*, November 1, 1995.

0022-3654/95/2099-17118$09.00/0

measure of proton transfer from the CO to the surrounding Ar atoms can be anticipated. The study is distinguished by several aspects from earlier ones of larger proton-bound complexes, e.g., $H_3^+-(H_2)_n$,[13] $H_3O^+-(H_2O)_n$,[14] and $NH_4^+-(NH_3)_n$.[15] In particular, as the ligands are atoms rather than molecules, the IR spectra are invitingly uncomplicated, prompting one to focus on the size development of several well-defined spectral features. A series of spectral properties are targeted including (1) the frequency of the HCO^+ ν_1 transition (i.e., the spectral solvent shift of the C−H stretch vibration), (2) frequencies for combination bands involving ν_1 and intermolecular vibrations, (3) photofragmentation branching ratios for production of different sized daughter ions, from which incremental binding energies are estimated within the framework of the statistical evaporation theory of Engelking,[18,19] and (4) the ν_1 band profiles. The range of cluster sizes characterized is also significant, extending to the completion of the first solvation shell at $n = 12$, and on to the beginning of the second shell at $n = 13$.

Eventually, one would hope to establish links between the experimental data and likely Ar_n-HCO^+ structures. For $n > 1$ the Ar_n-HCO^+ spectra are not rotationally resolved, obliging us to entertain indirect evidence in efforts to ascertain the disposition of the larger clusters' elements. In the tradition of previous studies of both neutral and ionic complexes, the regularities (and irregularities) in the development of particular cluster properties are connected with special cluster geometries. We discuss in turn the development of ν_1 vibrational band shifts, ν_1 band profiles, intermolecular frequencies, and Ar atom binding energies as a function of cluster size. It is perhaps important to emphasize at the outset that without rotationally resolved spectra for the larger clusters, the structural conclusions are to some extent tentative.

To guide structural considerations for the larger Ar_n-HCO^+ clusters, minimum energy geometries are calculated by employing simple atom−atom pair potentials, supplemented by charge-induced dipole terms and second-order interactions between the induced dipoles. While the form of the potential energy function is crude, useful structural insights are derived. In particular, it is found that discontinuities in the development of certain cluster properties can be associated with the completion of Ar solvation rings disposed equatorially about the linear $Ar-HCO^+$ core.

Significantly, the Ar_1-HCO^+ ν_1 spectrum *is* rotationally resolved and so provides fundamental information on the interaction potential between an Ar atom and the HCO^+ molecular ion in regions adjacent to the potential minimum. Although a full analysis is not yet complete, information on the minimum energy geometry and intermolecular bond strength is obtained that can be compared to data for other recently characterized proton-bound dimers ($He-HCO^+$,[20] $He-HN_2^+$,[21] H_2-HCO^+,[22] and $H_2-HN_2^+$ [23]). The minimum energy structure for these species appears to be one where the ligand interacts most effectively with the proton: a linear complex for rare-gas-containing complexes, and a C_{2v} T-shaped one when hydrogen is the ligand.

This paper is organized as follows. First comes a short description of the experimental approach. This is followed by analysis and discussion of the $Ar-HCO^+$ dimer ν_1 spectrum and its implications for the structure of the dimer and nature of the $Ar\cdots HCO^+$ intermolecular interaction. For the bigger clusters, the Ar_n-HCO^+ minimum energy geometries are first calculated, before proceeding to analyze and discuss the spectra. Finally, we consider and summarize the salient points.

II. Experiment

Vibrational spectra of size-selected Ar_n-HCO^+ cluster ions are obtained by photoexciting cluster vibrational resonances lying above the dissociation threshold, with absorption being inferred through the observation of ionic photoproducts. The apparatus is in essence a tandem mass spectrometer, consisting of an electron impact cluster ion source, a quadrupole mass filter for primary selection of the desirable parent species, an octopole ion guide in which the cluster ions meet the counterpropagating tunable IR beam, and a second quadrupole mass filter set to the photofragment mass. Fragment ions are eventually detected with a Daly scintillation detector[24] coupled to a gated boxcar integrator. The machine's application to the electronic spectroscopy of mass-selected cluster ions has been recently reviewed.[25] The only significant change in the experimental setup compared to the one used for an earlier mid-infrared study of H_2-HCO^+ [22] is the incorporation of an InAs infrared detector for signal normalization by laser power.

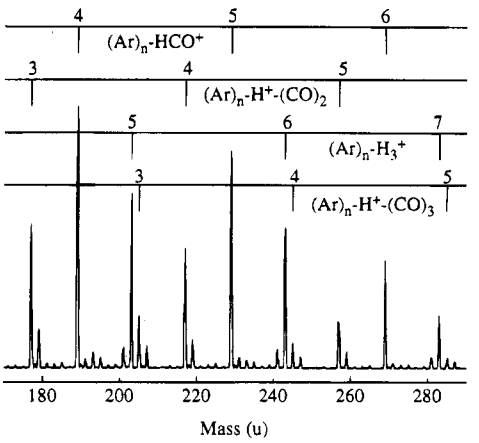

Figure 1. Portion of mass spectrum for cluster ions produced by the electron impact−supersonic expansion ion source.

The cooled cluster ions are produced in a pulsed supersonic expansion of H_2, CO, He, and Ar crossed by an electron beam. The gas composition was optimized with an on-line gas mixer and eventually a H_2:CO:He:Ar ratio of 2:1:50:100 at 4−7 bar stagnation pressure was employed. A variety of heterogeneous cluster ions issue from the source, the dominant series being $Ar_n-H_3^+$ and $Ar_n-H^+-(CO)_m$ (Figure 1). Introduction of He into the octopole region of the apparatus facilitates the identification and optimization of the desired Ar_n-HCO^+ parent species through the monitoring of collision induced $Ar_{n-1}-HCO^+$ fragments. As expected, an increase in either the stagnation pressure or the proportion of Ar in the gas mixture shifts the Ar_n-HCO^+ ion distribution toward a higher degree of solvation. In all cases, the resolution of the initial and final quadrupole stages was adjusted so that parent and daughter masses were clearly resolved. Unfortunately, an upper limit on the mass transmitted by the first quadrupole (≈560 u) precludes characterization of Ar_n-HCO^+ clusters larger than $n = 13$.

The light source is a commercial, seeded optical parametric oscillator (OPO) system (Continuum Mirage 3000) capable of producing tunable light in the mid-infrared with a bandwidth of less than 0.02 cm^{-1}. Calibration of rotational lines in the $Ar-HCO^+$ ν_1 band was achieved by simultaneously recording optoacoustic spectra of either N_2O (excited by the mid-infrared OPO output) or a C_2H_2/HDO mixture (excited by the near-infrared output).[26] The ions pass through the octopole with an energy of around 4 eV, necessitating a small Doppler correction to the measured wavenumbers (0.032 cm^{-1} at 2815 cm^{-1}). By using the octopole ion guide as a retarding field energy analyzer, an energy spread of approximately ±1 eV was determined for the parent ion beam, implying a Doppler width of roughly 0.008 cm^{-1} at 2815 cm^{-1} for $Ar-HCO^+$.

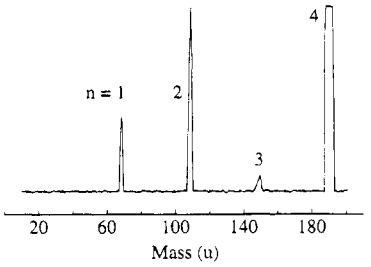

Figure 2. Mass spectrum of daughter ions arising from the Ar_4-HCO^+ parent ion when the laser is tuned to the ν_1 band. Whereas practically all of the Ar_1-HCO^+ and Ar_2-HCO^+ ions result from laser action, the Ar_3-HCO^+ signal is a consequence of metastable decay and collision-induced dissociation.

Generally, exposure of a particular sized Ar_n-HCO^+ cluster to IR photons leads to the production of several different sized daughter ions, often with the branching ratio depending sensitively upon the photon frequency. Figure 2 shows a mass spectrum of daughter ions arising from Ar_4-HCO^+ when the laser is tuned to the peak of the ν_1 band. Whereas practically the entire Ar_1-HCO^+ and Ar_2-HCO^+ signals are due to laser action, the Ar_3-HCO^+ ions are a consequence of metastable decay and collision-induced dissociation. To compensate for any background signals the ion source was pulsed at twice the laser frequency (20 Hz), with the laser-off signal being subtracted from the laser-on signal.

While under normal experimental conditions the power dependence of the photoinduced signal was found to be linear, implying that multiphoton processes were not of great significance, in larger clusters the effects of two photon absorption are discernible. For example, when the $Ar_{12}-HCO^+$ cluster is irradiated at the peak of its ν_1 absorption, the daughter product distribution is bimodal. Whereas Ar_7-HCO^+ and Ar_8-HCO^+ constitute the major photoproducts, Ar_4-HCO^+ is also formed ($\approx$0.5% of the Ar_8-HCO^+ signal under typical conditions). The secondary $n = 4$ channel can be convincingly explained as arising from a two-photon absorption by $Ar_{12}-HCO^+$, as both Ar_7-HCO^+ and Ar_8-HCO^+ photodissociate predominantly into Ar_4-HCO^+ (see below).

Depending on their size, parent clusters enter the octopole some 80–200 μs after formation in the ion source with 4 eV of translational energy in the laboratory frame. Metastable decay and collision-induced fragmentation of the clusters are assessed by allowing them to collide with N_2 or He background gas admitted in the octopole region. Monitoring the $(Ar_{n-1}-HCO^+)/(Ar_n-HCO^+)$ ratio as a function of the background pressure provides an estimation of the metastable fraction from the intercept of the Stern–Volmer plot. The results can be summarized as follows: (1) in the 80–200 μs time window, the metastable fragmentation fraction increases with cluster size; (2) decomposition into the $n - 1$ channel predominates; (3) even for the largest clusters investigated (Ar_8-HCO^+), only around 1% of the clusters decompose (see Figure 2 for $n = 4$). The relatively small decomposition fraction may be due to the fact that in the supersonic ion source the clusters are probably produced in a process of Ar accretion onto cool molecular ion cores with subsequent third-body stabilization, rather than through electron impact ionization of preformed neutral clusters.

In an effort to ascertain whether disintegration following ν_1 excitation occurs on time scales longer than the typical flight time through the octopole region, measurements of daughter photofragment branching ratios were taken with different parent translational energies. For example, in one experiment $Ar_{10}-HCO^+$ was introduced into the octopole with either an energy of 4.0 or 0.5 eV (corresponding to octopole flight times of roughly 250 and 750 μs, respectively) and irradiated at the ν_1 maximum. It was found that the branching ratio for production of Ar_5-HCO^+ and Ar_6-HCO^+ was the same within experimental error (±5%) at both energies, suggesting that the dissipation/evaporation process transpires on a time scale of less than 100–200 μs. Possibly the fragmentation processes could be investigated directly using an apparatus with a shorter effective time window.

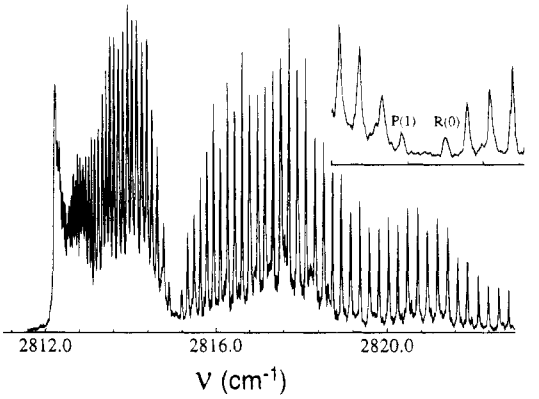

Figure 3. Mid-infrared spectrum of the $Ar-HCO^+$ ν_1 band recorded at 0.02 cm^{-1} resolution by detecting HCO^+ predissociation products as the OPO frequency is scanned. The inset shows the band-gap region with its obvious 4B spacing. The structure underlying part of the R branch transition is presumably due to a sequence band involving the *intermolecular* bending mode. The intensity distribution of the rotational lines is consistent with a rotational temperature of roughly 35 K.

III. $Ar-HCO^+$: Results and Analysis

Although in the course of these investigations at least five separate rotationally resolved bands have been identified, the present work is mainly concerned with the most intense of these (Figure 3), a parallel ($\Sigma-\Sigma$) transition which is 5–10 times stronger than any other band lying within 300 cm^{-1} to lower or higher energy. The position, strength, and structure of the band immediately encourage its assignment to the ν_1 (C–H stretch) transition of the complex. A future publication will deal in more detail with the weaker combination bands.

Analysis of the $Ar-HCO^+$ ν_1 band proceeded by assuming a pseudodiatomic energy level expression for the ground and excited states, with the rotational energy levels expressed as an expansion in $J(J + 1)$. The P and R branch line positions up to $J = 34$ (calibrated positions available from the authors upon request) could be fitted to within the experimental accuracy with the expansion terminated at the second term:

$$\nu_{obs} = \nu_0 + B'[J'(J' + 1)] - D'[J'(J' + 1)]^2 - B''[J''(J'' + 1)] + D''[J''(J'' + 1)]^2 \quad (1)$$

Initially, the ground state B'' and D'' values were established by forming the appropriate combination differences. Subsequently, P and R branch line positions were fitted with B'' and D'' constrained to the combination difference values in order to obtain ν_0, B', and D'. The derived constants are listed in Table 1. Fitting of the P and R branch lines with B'' and D'' unconstrained yielded the same rotational constants (within the uncertainties) as those obtained from the combination differences method and did not significantly narrow the bounds for the centrifugal distortion constants. While the B values are determined to an accuracy of less than 0.2%, the uncertainties in the D values are of the same order as the fitted constants themselves. Slow scans at reduced power ($\leq$100 μJ/pulse) over

TABLE 1: Molecular Constants (in cm^{-1}) Determined for the ν_1 Band of Linear Ar−HCO^+ Using the Analysis Method Described in the Text[a]

state	ν	$B/10^{-2}$	$D/10^{-8}$
ground		6.646 (8)	7 (4)
ν_1	2815.063 (20)	6.829 (8)	17 (4)

[a] Two sigma confidence limits in the last digits of the constants follow each value in parentheses.

some of the more intense rotational lines demonstrate that the widths are laser limited (<0.02 cm^{-1}), permitting a lower limit of roughly 250 ps to be put on the ν_1 lifetime.

In a crude diatomic model, the B and D values can be linked to the radial attributes of the Ar···HCO^+ intermolecular bond. Neglecting zero point vibration and assuming an undistorted HCO^+ subunit, one deduces a proton−argon separation of 2.13 Å in the ground state and 2.08 Å in the excited state. Actually, upon complexation one might expect marginal proton transfer in the system, with a lengthening of the C−H bond. The intermolecular stretching frequency, ν_s, can be estimated by inserting the experimental B and D values into Millen's relationship[27]

$$\nu_s = \left[\frac{4B_{complex}^{3}}{D_{complex}}\left(1 - \frac{B_{complex}}{B_{HCO^+}}\right)\right]^{1/2} \quad (2)$$

(B_{HCO^+} = 1.488 cm^{-1} [28]). In the present case, the ground and upper state D values are poorly defined, making a precise determination of ν_s impossible. The lower limit for the ground state D value (3×10^{-8} cm^{-1}) corresponds to ν_s = 180 cm^{-1} and k_s = 37 N/m (k_s is the intermolecular stretch force constant), while the upper limit of the excited state D (21×10^{-8} cm^{-1}) corresponds to ν_s = 67 cm^{-1} and k_s = 5.3 N/m. The former values are compatible with the assignment of the band displaced 146 cm^{-1} to higher energy from ν_1 as the $\nu_1 + \nu_s$ combination.

The perils of directly relating B and D values to *radial* intermolecular properties, particularly in complexes consisting of an atom bound to an extended rodlike molecule, have been emphasized in studies on the Ar−HCN van der Waals molecule[29-31] (which is isoelectronic with Ar−HCO^+). While the potential energy surface for this neutral complex has a linear minimum, there is little encumbrance to the Ar moving about the core into a T-shaped configuration and zero point bending excursions are substantial. As the radial equilibrium distance between the constituents' centers of mass is significantly less in the T-shaped configuration than in the linear one, and as rotation tends to bring the intermolecular bond into alignment with the HCN axis, there is a marked rotational dependence of the effective rotational constant, manifesting itself as an anomalously large centrifugal distortion constant. Because the Ar···HCN anisotropy is of the same order as the HCN rotational constant, the van der Waals bending vibrations have considerable free rotor character: the $j = 0$ rotor state correlates with the ground state, and the $j = 1$ rotor level splits into Σ and Π bending states. Transitions from the ground state to these two bending states have been measured directly yielding frequencies of 5.5 and 6.1 cm^{-1}, respectively.[29,30] The ν_1 (C−H stretch) and $\nu_1 + \Pi_1$ (C−H stretch in combination with the Π intermolecular bend) bands have also been measured; in combination with ν_1, the van der Waals Π_1 bending frequency is only 8 cm^{-1}.[31]

Several questions can be asked concerning the nature of the Ar···HCO^+ intermolecular potential, particularly regarding the degree of anisotropy. Is there any appreciable barrier preventing the Ar from moving around into the T-shaped configuration? Are the severe angular−radial couplings noted for Ar−HCN also important in the isoelectronic Ar−HCO^+, or is the charged system more rigid? At this stage, without an analysis of the combination bands involving the intermolecular bending and stretching motions, it is not possible to definitely answer these questions. Here the following observations are merely made. (1) A weak band lying 17.5 ± 1 cm^{-1} above ν_1 seems to have the appropriate structure for the $\nu_1 + \nu_b$ combination band ($\nu_b \approx$ intermolecular bend), providing some evidence that the intermolecular bond is somewhat stiffer in Ar−HCO^+ than it is in Ar−HCN. A transition 146 cm^{-1} above ν_1 can be convincingly assigned as the $\nu_1 + \nu_s$ combination band ($\nu_s \approx$ intermolecular stretch). (2) The centrifugal distortion constant for Ar−HCO^+ is more than 1 order of magnitude smaller than it is for Ar−HCN (5.7×10^{-6} cm^{-1} [30]) again suggesting a less flexible bending coordinate for the Ar−HCO^+ ion. However, a labile bending coordinate would only be reflected in a large centrifugal distortion constant if the intermolecular equilibrium distance depends upon the bending angle.

The magnitude of the ν_1 vibrational band shift for Ar−HCO^+ (274 cm^{-1} to the red) is striking. In comparable neutral systems involving diatomic or triatomic molecules complexed with rare-gas atoms, vibrational shifts of just a few wavenumbers are typical. For example, the isoelectronic Ar−HCN van der Waals molecule features a ν_1 red shift of only 2.69 cm^{-1}.[31] In the Ar_n−HF series, the first Ar atom lowers the HF vibrational frequency by only 9.6 cm^{-1} (a relative shift of 0.24% of the HF vibrational frequency), and completely encasing the HF molecule in an Ar matrix still only produces a relative red shift of 1.1%.[8] In fact, the magnitude of the Ar−HCO^+ red shift is more akin to the ones for strongly hydrogen-bonded complexes (e.g., ≈245 cm^{-1} for ν_1 of HF−HCN), emphasizing the substantial interaction between the HCO^+ cation and the linearly disposed Ar atom. Presumably the fact that the proton is attracted by both the CO *and* the Ar (ArH^+ is a strongly bound species, $D_0 \approx$ 31 000 cm^{-1} [17]) results in a flattened effective proton potential and a reduced characteristic frequency for its motion.

Another perspective on vibrational band shifts in weakly bound complexes is provided by models that seek to explain the shifts in terms of differences in the monomer−monomer electrostatic and polarization energies in the two vibrational states.[32] By taking into account the internal coordinate dependence of the monomer multipole moments and the anharmonicity of the molecular vibrations, such an approach has successfully accounted for shifts in a number of hydrogen-bonded species.[32] Can such an approach explain the vibrational band shifts for (rare-gas)−HCO^+ complexes? In this case, the dominant attractive contribution arises from the polarization of the rare gas (Rg) by the HCO^+ charge distribution, a contribution that is proportional to the rare-gas polarizability. Thus, the difference in the polarization energies for ground and ν_1 states (i.e., the band shift) should scale linearly with the rare-gas polarizability. The existing experimental data are not entirely consistent with this expectation. Rotational analysis of the ν_1 spectra of He−HCO^+,[20] Ne−HCO^+,[33] and Ar−HCO^+ demonstrates that while all three species have similar intermolecular separations (respectively 2.00, 1.98, and 2.13 Å assuming an undistorted HCO^+), the ratio of vibrational band shifts (1:3.4:22) differs significantly from the ratio of rare-gas polarizabilities (1:1.9:7.8). Although there will also be second-order contributions that scale with the square of the rare-gas polarizability, principally between the induced dipole moment on the rare-gas atom and the dipole moment induced on the HCO^+ core by this induced rare-gas dipole, rough calculations suggest that

these are at least 1 order of magnitude smaller than the first-order induction contributions and are not large enough to account for the observed discrepancy. The difference between the expected and observed band shifts is possibly due to appreciable monomer charge reorganization attending complex formation, rendering an electrostatic model based solely on monomer properties inappropriate. As well, vibrational mediation of the intermolecular overlap repulsion may contribute significantly to the band shift.

IV. Larger Ar_n-HCO^+ Clusters

(a) Structures. To help clarify issues surrounding the structure of the larger Ar_n-HCO^+ complexes, we begin by calculating minimum energy configurations using a simple semiempirical form for the potential energy function. The calculations are not intended to provide quantitatively accurate values for bond distances and bond energies, but rather to generate probable cluster configurations which can serve as foci for subsequent discussion of the development of vibrational band shifts, bandwidths, and combination band spacings and binding energies with cluster size.

For the Ar_n-HCO^+ clusters the total cluster potential energy (V_{tot}) is represented as a sum of atom−atom Lennard-Jones (12-6) type terms (V_{LJ}), supplemented by charge-induced dipole (cid) contributions (V_{cid}) and second order charge induced dipole-charge induced dipole interactions (cid−cid) between the Ar atoms ($V_{cid-cid}$):

$$V_{tot} = V_{LJ} + V_{cid} + V_{cid-cid} \tag{3}$$

A similar approach has been employed on previous occasions to explore geometries, binding energies, and vibrational frequencies for benzene cation−(Rg) complexes and transition metal−(Rg) complexes,[34,35]

It should be pointed out that such a simple potential function has deficiencies. For example, it ignores the influence of the higher order electrical moments of the HCO^+ core (dipole, quadrupole, etc.) and so does not take into account their polarization interactions with the argons. Furthermore, in seeking to represent the repulsive part of the potential by a r^{-12} term with a coefficient appropriate to the interaction of neutral species it ignores the presence of incipient chemical effects which may serve to ameliorate the effects of overlap repulsion. Significantly, the potential would predict an incorrect T-shaped geometry for the $Ar-HCO^+$ dimer, which the IR spectra show to be linear. In addition, even if the argon atom in the dimer is constrained to lie on the HCO^+ axis, the equilibrium Ar···H distance predicted from consideration of the Lennard-Jones and induction terms (assuming a single positive charge centered between the C and H atoms) greatly exceeds the experimentally obtained one (3.02 Å compared to 2.13 Å).

In order to partially account for deficiencies noted in the previous paragraph, it was assumed that the Ar_n-HCO^+ clusters are built up by addition of Ar atoms to a frozen linear $Ar-HCO^+$ core whose geometry is derived from the dimer spectrum (section III). The C−O and C−H bond lengths are taken from spectroscopic studies of HCO^+ [36] (1.105 and 1.097 Å, respectively) while the H−Ar displacement is deduced from the analysis in section III (2.13 Å).

The Lennard-Jones part of the potential is the sum of a number of Ar−(core atom) and Ar−Ar interactions:

$$V_{LJ}(r_{AB}) = 4\epsilon_{AB}\left(\left(\frac{\sigma_{AB}}{r_{AB}}\right)^{12} - \left(\frac{\sigma_{AB}}{r_{AB}}\right)^{6}\right) \tag{4}$$

TABLE 2: Lennard-Jones Pairwise Interactions Parameters (σ and ϵ) Employed for the Calculation of Ar_n-HCO^+ Minimum Energy Configurations

A−B	ϵ_{AB} (cm^{-1})	σ_{AB} (Å)
Ar−Ar[a]	111.32	3.343
Ar−H[b]	33.0	3.21
Ar−C[b]	40.2	3.42
Ar−O[c]	89.0	3.10

[a] Reference 37. [b] Reference 38. [c] $\sigma_{O-Ar} = {}^1/_2(\sigma_{O-O} + \sigma_{Ar-Ar})$ and $\epsilon_{O-Ar} = (\epsilon_{O-O}\,\epsilon_{Ar-Ar})^{1/2}$ with σ_{O-O} and ϵ_{O-O} taken from ref 39.

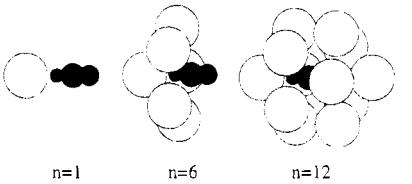

Figure 4. Calculated minimum energy structures for Ar_1-HCO^+, Ar_6-HCO^+, and $Ar_{12}-HCO^+$. The dimer structure is determined from rotational analysis of its ν_1 transition. Structures for the two larger clusters have been calculated assuming a frozen Ar_1-HCO^+ core and using the semiempirical potential described in section IVa.

Relevant σ and ϵ parameters for the pairwise interactions are given in Table 2.

The charge-induced dipole (cid) interaction between the positive charge q and an Ar atom with polarizability α (which dominates the attractive part of the potential) is given by

$$V_{cid}(r) = -\frac{1}{2}\frac{\alpha q^2}{(4\pi\epsilon_0)^2 r^4} \tag{5}$$

with $\alpha/(4\pi\epsilon_0) = 1.642 \times 10^{-30}$ m^3.[40] For most of the calculations, a single positive charge located midway between the hydrogen and carbon atoms was assumed. If the charge is positioned at the origin, the interaction between the induced dipoles on two Ar atoms is given as

$$V_{cid-cid}(\tilde{r}_{ij},\tilde{r}_i,\tilde{r}_j) = \frac{1}{4\pi\epsilon_0}\left(\frac{\tilde{\mu}_i(\tilde{r}_i)\cdot\tilde{\mu}_j(\tilde{r}_j)}{r_{ij}^{\,3}} - 3\frac{(\tilde{\mu}_i(\tilde{r}_i)\cdot\tilde{r}_{ij})(\tilde{\mu}_j(\tilde{r}_j)\cdot\tilde{r}_{ij})}{r_{ij}^{\,5}}\right) \tag{6}$$

with induced dipole moments

$$\tilde{\mu}_i(\tilde{r}_i) = \frac{\alpha q}{4\pi\epsilon_0}\frac{\tilde{r}_i}{r_i^{\,3}} \tag{7}$$

For two Ar atoms separated by 3.75 Å (approximately the Ar_2 equilibrium distance) and both situated 3.0 Å from a single positive charge, the cid−cid interaction energy amounts to +52.3 cm^{-1}, which is of the same order as the well depth for the Ar···Ar interaction (see Table 2).

Using the potential energy function described above, the energy minimization for the Ar_n-HCO^+ ($n = 2-13$) series was accomplished using the downhill simplex method.[41] As expected, the minimum energy cluster geometries (see Figure 4 for $n = 1$, 6, and 12) were those that optimized the charge-induced dipole interaction between the positive charge and the Ar atoms. The first five Ar atoms added to the $Ar-HCO^+$ core form a primary solvation ring, equatorially disposed about the C−H bond midpoint (the position of the positive charge). Addition of a further Ar atom begins a second solvation ring, which is staggered with respect to the first and is completed at $Ar_{11}-HCO^+$. A 12th Ar atom sits over the oxygen end of the cluster so completing the primary solvation shell. For clusters up to $Ar_{12}-HCO^+$ the powerful charge-induced dipole forces

TABLE 3: Ar Binding Energies for the Ar_n-HCO^+ Series[a]

n	$D(n)/cm^{-1}$ (calc)	$D(n)/cm^{-1}$	$D(n)/cm^{-1}$ (low KE)
1		910	1200
2	955	790	940
3	980	950	1010
4	965	880	1040
5	950	840	920
6	945	610	660
7	595	520	500
8	680	510	590
9	690	620	590
10	690	480	580
11	780	690	610
12	735	550	680
13	488	360	410
ϵ		0.372	0.025

[a] Values given in the second column were calculated using the simple pairwise potential augmented by polarization and induced dipole–induced dipole interactions as described in section IVa. The third and fourth columns give incremental binding energies $D(n)$ for Ar_n-HCO^+ complexes determined from a least-squares fitting of the photofragmentation branching ratios using the procedure described in section IVb(iv). Binding energies were determined using an Engelking approach (3rd column), or a modified approach where the first Ar departs with almost zero kinetic energy (4th column). The ϵ value is the sum of the squared differences between the modeled and the observed branching ratios (a smaller value implies a better fit). The second and fourth columns are plotted in Figure 6c.

ensure that no matter the starting configuration for the geometry optimization, the clusters find their way to the same minimum. However, for $Ar_{13}-HCO^+$ there are several distinct isomers with similar minimum energies (within 60 cm^{-1}) which are separated by appreciable isomerization barriers. The 13th Ar atom can be either located between one of the solvation rings and a terminal Ar atom at either the proton or oxygen end (total cluster binding energies of −9452 cm^{-1} and −9394 cm^{-1}, respectively), or alternatively positioned between the primary and secondary solvation rings, with the additional Ar atom coordinated with two Ar atoms in the first ring and one in the second (−9410 cm^{-1}) or *vice versa* (−9421 cm^{-1}).

The calculated incremental binding energies, along with the values obtained from the photofragmentation branching ratios (*vide infra*), are summarized in Table 3. From the perspective of the model potential calculations, the lower binding energies for Ar atoms in the second solvation ring compared to those in the first reflect their greater displacement from the center of charge, and the consequently smaller cid interaction. Within the first ring, the incremental binding energies are roughly constant for all five Ar atoms. This comes about because the attractive Lennard-Jones interactions are balanced by roughly equal cid–cid repulsive ones. In the second ring, which is further away from the charge center, the repulsive cid–cid interaction is smaller and is overridden by the dispersion forces. This results in a small increase in the incremental binding energies between $n = 7$ and $n = 11$.

In order to test the effect of distributing the positive charge over the HCO^+ core, minimum energy geometries were also calculated with Mulliken charges taken from ref 42 (+0.3865 on H, +0.619 on C, −0.0055 on O). The principal consequence was an increase in the stepwise binding energies of the Ar atoms in the second solvation ring, although cluster structures and the form of the binding energy versus cluster size plot were almost unchanged. A yet more appropriate description of the HCO^+ charge distribution would involve distributing multipoles over several molecular sites.[43]

(b) Experimental Results and Analysis. Figure 5 depicts infrared vibrational predissociation spectra of mass selected

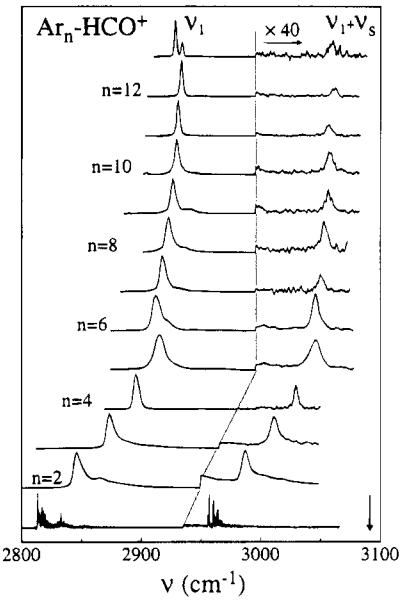

Figure 5. Infrared vibrational predissociation spectra of mass selected Ar_n-HCO^+ ($n = 1-13$) clusters. The spectra were taken by monitoring the dominant photofragmentation product (listed in Table 4). Note that the right-hand part of the spectrum has been expanded by a factor of 40 to allow a clear view of the $\nu_1 + \nu_s$ band. The position of the free HCO^+ ν_1 transition (3088.7 cm^{-1}) is marked with an arrow.

Ar_n-HCO^+ ($n = 1-13$) clusters obtained in the manner described in section II. For almost all cluster sizes, absorption of an infrared photon in the 2800–3100 cm^{-1} range results in the formation of only one or two different sized daughter fragments, with the branching ratio depending on the IR frequency. Generally, for the smaller clusters, where photofragmentation proceeds into two channels, predissociation spectra were recorded at both fragment masses (in Figure 5 the dominant mass channel spectra are shown). In the following subsections we present and discuss in turn data relating to the ν_1 vibrational band shifts, the ν_1 band profiles, the relative positions of the combination bands, and the photofragment branching ratios (this information is summarized in Tables 4 and 5). The focus for much of the discussion is on the relationship between the data and Ar_n-HCO^+ structures.

(i) ν_1 Band Shifts. As can be seen by inspecting Figure 5, the spectra for $n \leq 12$ are dominated by a predominant, relatively sharp band (fwhm < 10 cm^{-1}), almost certainly associated with the chromophore HCO^+ ν_1 vibration. Significantly, for $Ar_{13}-HCO^+$ *two* peaks separated by ≈5.8 cm^{-1} are apparent. The shifts in the ν_1 band, plotted as a function of cluster size in Figure 6a, vary in a fairly systematic fashion as the number of Ar atoms in the cluster increases. While addition of the first Ar atom results in a massive 274 cm^{-1} displacement to lower energy of ν_1 from the free molecule value, adding more Ar atoms brings the transition almost monotonically back to higher energy, so that for example at $n = 12$ the total red shift is only 156 cm^{-1}. For the larger clusters the *incremental* shifts (i.e., the displacement of the Ar_n-HCO^+ ν_1 transition from the one of $Ar_{n-1}-HCO^+$) are modest and are generally back to the blue (higher energy), although between $n = 5$ and $n = 6$ there is a small incremental red shift. For $n = 2-5$ the incremental blue shift is roughly 25 cm^{-1} per Ar atom, while for $n = 6-12$ it is only around 4 cm^{-1} per Ar atom (see Table 4 and Figure 6a).

In the past, vibrational and electronic band shifts for neutral van der Waals molecules have been related to cluster structures within the framework of the band shift rule. First formulated to explain the observation that electronic solvent shifts in I_2

TABLE 4: Spectral and Branching Ratio Data for Mid-infrared Transitions of Ar_n–HCO^+ (n = 1–13) Clusters[a]

n	n_d	ν_1 (cm^{-1})	$\Delta\nu_{inc}$ (cm^{-1})	$\nu_1 + \nu_s$ (cm^{-1})	fwhm (cm^{-1})	% ν_1	% (calc) ν_1	% $\nu_1 + \nu_s$	% (calc) $\nu_1 + \nu_s$
0		3088.7[b]							
1	0	2815.1	−273.6	2961.0		100	100	100	100
2	0	2845.7	30.6	2986.3	7.7	95	100	100	100
2	1	2845.6			4.9	5	0	0	0
3	0				60	1	0	3	5
3	1	2872.7	27.0	3010.4	7.5	99	100	97	95
4	1	2896.8		3029.6	11.0	32	33	59	59
4	2	2895.1	22.4	3028.9	5.5	68	67	41	41
5	2	2914.6	19.5	3045.9	10.2	55	58	83	80
5	3	2916.5		3047.8	5.4	45	42	17	20
6	3	2911.9	−2.7	3045.5	7.7	99	95		
6	4					1	5		
7	3					6	10		
7	4	2917.0	5.1	3050.0	5.9	94	90		
8	4	2922.4	5.4	3052.9	6.1	90	86		
8	5					10	14		
9	4						3		
9	5	2926.1	3.7	3056.3	4.7	100	97		
10	5	2929.3	3.2	3057.7	4.1	68	70		
10	6	2928.4			3.4	32	30		
11	6	2930.2	0.9	3056.9	2.8	92	92		
11	7					8	8		
12	7	2933.4	3.2	3061.4	2.3	70	69		
12	8	2933.2			1.8	30	31		
13	7						4		
13	8	2928.1	−5.3	3059.4	2.2	90	88		
13	9					10	8		
13	8	2933.9	0.5		2.2				

[a] Listed for each parent size (n) are the photodaughter sizes (n_d), the ν_1 frequency, the incremental ν_1 band shift $\nu_{inc}(n) = \nu_1(n) - \nu_1(n-1)$, combination band ($\nu_1 + \nu_s$) wavenumbers (given for each photofragment size where applicable), and measured photofragment branching ratios (for both bands). For n = 13 two peaks are apparent in the spectrum, the lower energy one of which is 2.5 times the intensity of the other (see Figure 5). The branching ratio data for n = 13 were recorded with the laser tuned to the more intense peak. Also given are the photofragment branching ratios calculated using the procedure outlined in section IVb(iv) (low kinetic energy release version) with the binding energies provided in the fourth column of Table 3. [b] From ref 44.

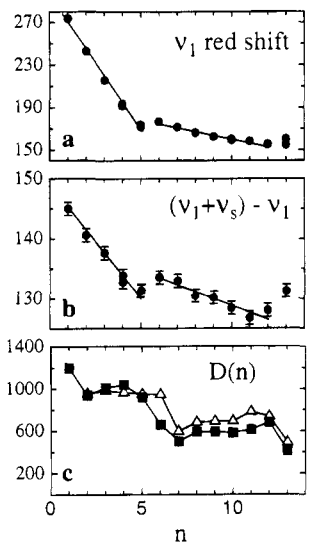

Figure 6. Development of Ar_n–HCO^+ properties (in cm^{-1}) as a function of cluster size. (a) Incremental ν_1 band shifts resulting from the addition of an Ar atom to the Ar_{n-1}–HCO^+ cluster (from Table 4). (b) The $(\nu_1 + \nu_s) - \nu_1$ separation (from Table 5). (c) Ar atom binding energies (Table 3). The two sets of points correspond to energies determined from (1) the calculations described in section IVa (triangles), (2) the photodaughter branching ratios using a modified Engelking model where the first Ar departs with close to zero kinetic energy (filled squares).

molecules complexed with rare-gas atoms increase more or less linearly with the number of attached ligands,[45] the rule implies that occupation of a particular solvent site leads to a well-specified displacement of the transition frequency. The band shift arising from the presence of a solvent atom depends upon its relative position with respect to the chromophore, and to first order is more or less independent of the presence of other solvent entities. Thus similar incremental shifts for addition of any two solvent atoms might be taken as evidence (although not proof) that they occupy equivalent positions with respect to the core.[45]

Within the framework of the band shift rule, the large red shift accompanying addition of the first Ar and the smaller constant ones for the ranges n = 2–5 and n = 6–12 are consistent with Ar_n–HCO^+ structures in which a single Ar atom adopts a priviledged, linear configuration (associated with the 274 cm^{-1} red shift), with subsequent Ar atoms completing first a primary solvation ring (where the blue shift averages 25 cm^{-1} per Ar atom) and then a secondary solvation ring (blue shift of 4 cm^{-1} per Ar atom), each containing four to five Ar atoms.

While the large red shift accompanying the addition of the first Ar atom presumably reflects a flatter effective proton potential (arising from the proton's tendency to move across onto the Ar atom), it may be asked why addition of Ar atoms to primary and secondary solvation rings about an Ar–HCO^+ core should lead to small incremental blue shifts. One explanation may be that in the larger complexes, the band shift is again determined principally by the terminal Ar atom, but that introduction of Ar atoms into the first solvation ring cause it to be pushed away from the proton. This should have the effect of diminishing its interaction with the proton, so leading to a reduced *total* red shift, i.e., an *incremental* blue shift. The same effect should accompany addition of Ar atoms to the second solvation ring, with members of the second ring nudging the first ring against the terminal Ar. The significantly smaller average incremental blue shift for n = 6 to n = 12 is consistent with such a second-order effect. The structure calculations described in section IVa also suggest that addition of Ar atoms to the second ring will press members of the first ring against

the terminal Ar atom; when both rings are filled, the first ring is displaced by approximately 0.4 Å (toward the terminal Ar atom) compared to its position when only the first ring is occupied.

Interestingly, for $Ar_{13}-HCO^+$ there are two ν_1 bands, the smaller one of which is virtually undisplaced from the $Ar_{12}-HCO^+$ peak (0.5 cm^{-1} blue shift), while the other more intense one is red-shifted by 5.3 cm^{-1}. It is tempting to associate the latter of these with an $Ar_{13}-HCO^+$ isomer in which the 13th Ar atom is the first member of the second solvation shell and is positioned at the proton end of the cluster where due to favorable induction interactions it should be most firmly bound. In such a position it is liable to *compress* the bond between the linearly positioned Ar atom and the proton, so producing the observed incremental red shift. On the other hand, the undisplaced peak may be associated with one or more of the other three possible isomers where the 13th Ar atom is between the two solvation rings or at the oxygen end. In these other sites, the additional Ar atom should have little direct interaction with the proton-bound Ar atom and so should effect a smaller change in the ν_1 frequency.

The observed ν_1 band shifts are more difficult to reconcile with alternative Ar_n-HCO^+ structures. For example, consider a T-shaped C_{2v} structure for the Ar_2-HCO^+ trimer in which the proton is shared by the CO molecule with *two* equivalent Ar atoms. Under such circumstances, the further delocalization of the proton would be expected to result in a lower characteristic frequency compared to the $Ar-HCO^+$ dimer. One would therefore anticipate an incremental *red* shift accompanying addition of the second Ar atom, contrary to the observed incremental *blue* shift. Similarly for a C_{3v} Ar_3-HCO^+, with the proton directed at the center of an equilateral triangular Ar_3 unit in which the proton is shared by the CO with three equivalent Ar atoms, one would expect an even lower characteristic ν_1 frequency and again, contrary to observation, an incremental red shift. Furthermore, the almost equal incremental blue shifts for Ar_2-HCO^+ to Ar_5-HCO^+ strongly suggest that the second to the fifth Ar atoms are being added to roughly equivalent positions, which is not consistent with C_{2v} and C_{3v} trimer and tetramer structures.

It is of some interest to compare the vibrational band shifts of the Ar_n-HCO^+ clusters and ones of the Ar_n-HF ($n = 1-4$) van der Waals molecules for which the minimum energy structures are known from both microwave[6,46-48] and infrared studies[49,50] to be C_{2v} for the trimer, C_{3v} for the tetramer, and C_{3v} for the pentamer (proton pointed to the base of an Ar_4 tetrahedron). In contrast to Ar_n-HCO^+, the Ar_n-HF ($n = 1-4$) series exhibits incremental shifts which are always to the red, a situation which persists up to $n = 12$ if recent rovibrational calculations which reproduce the smaller cluster red shifts are correct.[51] Significantly, the predicted band shift for $Ar_{12}-HF$ (corresponding to the complete encasement of the HF in a solvation sphere) is already close to the one for HF trapped in an Ar matrix. Unfortunately, at present there appear to be no corresponding Ar matrix data for HCO^+.

(ii) ν_1 Band Profiles. Inspection of the Ar_n-HCO^+ spectra demonstrates that the ν_1 band profiles depend sensitively upon both the size of the parent cluster and also upon which photodaughter mass is monitored. Invariably the ν_1 peak recorded on the smaller daughter channel is broader than on the larger mass channel and often exhibits a shoulder extending 10–20 cm^{-1} to higher energy from the main peak. This behavior is illustrated in Figure 7 where spectra of Ar_n-HCO^+ ($n = 2-5$, 10, and 12), recorded on the higher and lower mass fragmentation channels are shown. In some cases, there are

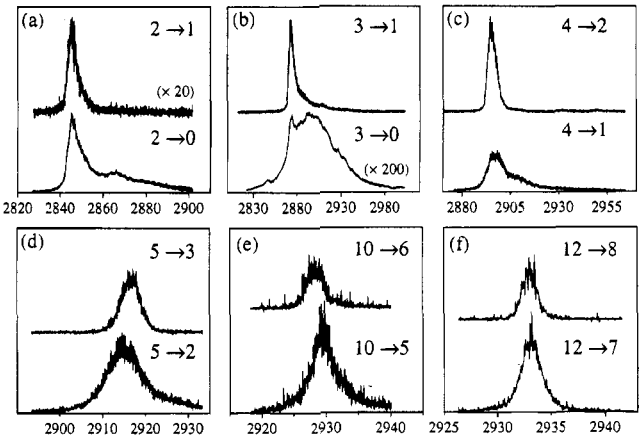

Figure 7. The ν_1 bands of Ar_n-HCO^+ ($n = 2$, 3, 4, 5, 10, and 12) taken on two different mass channels. In all cases the spectrum recorded on the smaller daughter mass is broader. The fine structure in the larger cluster spectra is not reproducible. Energies are given in cm^{-1}.

extreme differences between the spectra, particularly when the probability for dissociation into the lower mass channel is small. For example, the Ar_3-HCO^+ spectrum recorded on the dominant $3 \rightarrow 1$ channel is relatively sharp (fwhm $\approx$ 7.5 cm^{-1}) compared to the very much broader $3 \rightarrow 0$ one (fwhm $\approx$ 60 cm^{-1}), although the latter retains a sharp peak at the same position as the former (see Figure 7b).

A number of different effects probably contribute to the ν_1 profiles. For the smaller clusters, the rotational constants should be large enough to produce reasonably broad rotational contours. In fact, rigid rotor simulations of the Ar_2-HCO^+ spectrum using rotational constants corresponding to the calculated geometry suggest that resolved rotational structure should be just apparent with the 0.02 cm^{-1} bandwidth light source. Its absence may be due either to homogeneous line broadening caused by rapid vibrational relaxation/predissociation or to congestion arising from hot bands or isomers. Although the $Ar-HCO^+$ lines are unbroadened at the 0.02 cm^{-1} experimental resolution, it is possible that the presence of an additional Ar atom hastens the flow of energy from ν_1 into the intermolecular modes.

Interestingly, it is one of the largest clusters characterized, $Ar_{12}-HCO^+$, which displays the narrowest ν_1 contour. In this case, the width of the band (1.8 cm^{-1}) provides a rough 3 ps *lower* bound for the upper state vibrational relaxation/predissociation lifetime. As relaxation from the ν_1 level is unlikely to be faster in clusters with fewer Ar atoms, one is encouraged to suppose that most of the broadening in the smaller clusters' spectra is due to heterogeneous effects rather than homogeneous lifetime broadening.

One obvious cause for heterogeneous ν_1 broadening may be the presence of closely spaced sequence bands arising from clusters endowed with some measure of energy in the low frequency intermolecular motions. Sequence transitions (hot bands) involving these intermolecular vibrations will be displaced slightly from the ν_1 transition due to cross anharmonicity. Cluster temperatures (about 30–40 K if they are the same as the rotational temperature of $Ar-HCO^+$) are almost certainly high enough for the intermolecular vibrational modes to be populated. Following infrared absorption, clusters which were initially hot will possess more energy than initially cold ones, and so on average will shed more Ar atoms, thus explaining the occurrence of broader ν_1 bands on the deeper mass channel. Blue-shifted sequence bands would imply that excitation of the C–H stretch vibration *raises* the frequency of the intermolecular vibrations (i.e., there is positive cross anharmonicity). This is

consistent with observations for the Ar−HCO^+ dimer, where exciting the C−H stretch vibration (ν_1) leads to a *contraction* of the intermolecular bond and presumably to an increase in the intermolecular frequencies (a ν_1 mediated increase in the intermolecular bond strength has been noted in other proton-bound complexes[20−22]).

Following a similar line of reasoning the observation that the ν_1 bandwidths diminish with cluster size can also be explained. The intermolecular modes most strongly coupled to ν_1 will primarily be ones associated with the Ar atoms closest to the proton, particularly the Ar atom lying on the HCO^+ axis. Addition of Ar atoms to the primary and secondary solvation rings should serve to support the terminal Ar atom so raising its characteristic frequencies. Thus at a given temperature, modes strongly coupled with ν_1 are less likely to be populated in the larger clusters.

The decrease in ν_1 contour widths for the larger clusters may also be linked to cluster vibrational temperatures that diminish with increasing cluster size. While generally for small ionic clusters and complexes, the electron impact cluster ion source generates species with rotational temperatures of roughly 30−40 K[25,53] (consistent with the intensity distribution of the Ar−HCO^+ rotational lines in Figure 3), it is not clear that temperatures for small and large clusters will be identical. It is also conceivable that part of the ν_1 broadening arises from the presence of several isomers for each cluster size. The most stable isomer may then give rise to the relatively sharp feature which dominates the spectrum recorded on the higher mass channel, while other less stable isomers having slightly different ν_1 absorption frequencies undergo more extensive fragmentation to produce the broader spectrum observed on the deeper mass channel.

(iii) Combination Bands. Lying some way to higher energy (20−200 cm^{-1}) from the ν_1 band are weaker transitions that can be tentatively assigned as combinations involving ν_1 and intermolecular vibrational motion(s). One of these peaks, which can be seen in all of the $n = 1-13$ spectra, is separated from ν_1 by roughly 130−140 cm^{-1} and is likely due to a combination of ν_1 and the *intermolecular* stretching vibration (ν_s). The $\nu_1 + \nu_s$ band has been observed in He−HN_2^+ where it is separated by roughly 163 cm^{-1} from ν_1. The alternative possibility, that the band arises from an *intramolecular* HCO^+ combination band (e.g., $\nu_2 + \nu_3$ which should lie close by, *ca.* 3012 cm^{-1} [54]), seems improbable given the weak bands' more or less constant displacement from ν_1 for the entire Ar_n−HCO^+ series. If the band was in fact the $\nu_3 + \nu_2$ combination, its displacement from the free molecule position would be to lower energy for the smaller clusters ($n \leq 3$) and to higher energy for the larger ones ($n > 3$).

In addition to the aforementioned bands, between $n = 4$ and $n = 7$ there are two weaker bands apparent in the spectrum, one displaced from ν_1 by between 30 and 40 cm^{-1} and the other by between 50 and 60 cm^{-1}. While the identities of these two bands are at present uncertain, they may possibly be associated with the intermolecular bending and stretching motions of equatorially disposed Ar atoms (see Figure 4). It is not clear why these bands are only visible in the $n = 4-7$ size range. The positions of the combination bands with respect to ν_1 are listed in Table 5.

The development of the $(\nu_1 + \nu_s) - \nu_1$ spacing with increasing cluster size, which is depicted in Figure 6b, can be seen to mirror the development of the vibrational band shifts (Figure 6a). Thus the stretch frequency diminishes almost linearly from $n = 1$ to $n = 5$ (3.4 cm^{-1} per Ar), increases slightly from $n = 5$ to $n = 6$, and again decreases roughly linearly from $n = 6$ to $n = 12$ (1.1 cm^{-1} per Ar). From $n = 12$ to $n = 13$ there is an increase in the ν_s frequency. Presumably the general decrease in the $(\nu_1 + \nu_s) - \nu_1$ spacing reflects a weakening of the intermolecular bond between the proton and the terminal Ar atom as further Ar atoms are added (although there may also be a small reduced mass contribution). Earlier it was suggested that the incremental blue shifts in the ν_1 bands were due to Ar atoms in primary and secondary solvation rings pushing the terminal Ar atom away from the proton and thereby diminishing its interaction with the HCO^+ core. The constant incremental decreases in the intermolecular stretching frequency for $n = 2$ to $n = 5$ and for $n = 6$ to $n = 11$ support a picture of the larger Ar_n−HCO^+ cluster being built up through the formation of primary and secondary solvation rings each containing 4−5 Ar equivalent atoms, with a progressive weakening of the bond between the terminal Ar and the HCO^+ core.

TABLE 5: Displacement of Minor Combination Bands from ν_1 in Ar_n−HCO^+ Clusters (in cm^{-1})[a]

n	$(\nu_1 + \nu_s) - \nu_1$	$(\nu_1 + \nu_a) - \nu_1$	$(\nu_1 + \nu_b) - \nu_1$
1	146		
2	141		
3	138		
4	134	55	37
5	131	57	39
6	134	54	33
7	133	55	33
8	130		30
9	130		
10	128		
11	127		
12	128		
13	131		

[a] The uncertainty in the displacements is ±1 cm^{-1}. While the ν_s vibration is probably the intermolecular stretching motion for the linearly positioned Ar atom, the other two vibrations' identities are at present uncertain. It is possible that they are associated with stretching and bending motions of the equatorially configured Ar atoms (see Figure 4). The $(\nu_1 + \nu_s) - \nu_1$ values are plotted as a function of cluster size in Figure 6b. The spacings are taken from spectra recorded on the dominant photodaughter channel.

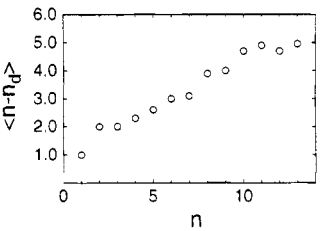

Figure 8. Average number of Ar atoms lost following excitation of ν_1 for the Ar_n−HCO^+ cluster series ($\langle n - n_d \rangle$). The data are taken from Table 4.

(iv) Dissociation, Branching Ratios, and Binding Energies. One of the striking features of the Ar_n−HCO^+ photofragmentation data is the extremely narrow range of photodaughter masses generated (Table 4), with most clusters decomposing to yield significant quantities of only one or two different sized photofragments. It can be seen in Figure 8, where the averaged evaporated number of Ar atoms is plotted as a function of cluster size, that for the bigger clusters ($n = 10-13$) around 5 Ar atoms are shed per IR photon (≈2930 cm^{-1}), corresponding to approximately 600 cm^{-1} per Ar. While it is tempting to claim this as the effective Ar binding energy for large clusters, further complications, relating to the internal energy of the clusters prior to IR absorption and also to the energy partitioned into the fragment kinetic energy, need to be addressed. Disregard of

energy flowing into the fragment translational kinetic energy will result in an overestimation of binding energies.

Two slightly different approaches were explored in an effort to model the Ar_n-HCO^+ photodissociation process taking into account the fragments' kinetic energy distributions. In the first, complete ν_1 energy randomization was assumed to occur prior to Ar atom evaporation, with Ar fragment kinetic energy distributions estimated at each evaporation stage within the framework of the approach developed by Engelking to model evaporation of CO_2 monomer units from photoactivated $(CO_2)_n^+$ clusters.[18,19] It is to be expected that the primary propagation of energy from ν_1 into the lower frequency cluster modes will be expedited to some extent by the presence of the HCO^+ core modes at 2184 cm^{-1} (ν_3) and 828 cm^{-1} (ν_2),[55] which should serve to alleviate the effects of energy-gap bottlenecks.

In the second approach, the first Ar atom was assumed to depart with close to zero kinetic energy, while kinetic energy distributions for subsequent evaporated Ar atoms were again modelled using the Engelking approach. For the vibrational predissociation of van der Waals molecules, it has been observed that channels minimizing fragment kinetic energy are often favored[56] and it is conceivable that a similar situation applies here. In the case of HCO^+, ν_1 and ν_3 differ by $\approx$905 cm^{-1}, possibly quite close to the binding energy of a single Ar atom, so primary ejection of a low kinetic energy Ar atom may be significant.

According to Engelking,[18,19] for a n-mer cluster possessing internal energy E, and with an incremental binding energy of $D(n)$, the probability R_i for evaporation into a channel with translational kinetic energy E_i is given by

$$R_i \propto E_i(E - D(n) - E_i)^{s-4} \tag{8}$$

where s is the number of active vibrations in the n-mer, here taken to be 3 times the number of Ar atoms in the cluster. Integration of the fragment kinetic energy over the distribution (eq 8) yields an average kinetic energy of[19]

$$E_{av} = 2(E - D(n))/(s - 1) \tag{9}$$

Thus, as the size of the disintegrating cluster increases, less energy is partitioned into fragment translational kinetic energy.

Initially, the clusters are assumed to have internal temperatures of 35 K (corresponding roughly to the distribution of the $Ar-HCO^+$ rotational line intensities in Figure 3), with an energy distribution given by $P(E) \propto \exp(-E/kT)^*\rho(E)$, where $\rho(E)$ is the classical density of states for a collection of harmonic oscillators

$$\rho(E) = E^{s-1}/(s - 1)!\prod_{j=1}^{s} h\nu_j \tag{10}$$

Although, prior to IR photon absorption, the larger clusters may have sufficient energy to decompose, estimations of the rates using RRK theory indicate that disintegration is practically insignificant during the experimental time window. Absorption of an IR photon shifts the clusters' energy distribution upward by the photon energy so that replete with the additional energy the clusters proceed to fragment.

One additional complication preventing the immediate application of eq 8 to the determination of photodaughter branching ratios, is connected to the fact that clusters possessing energy in excess of the dissociation threshold do not necessarily fragment on the experimental timescale (<1 ms). To take this into account, decomposition rates are calculated at each fragmentation stage using the RRK expression,

$$k(E) = \beta\nu\left(\frac{E - D(n)}{E}\right)^{s-1} \tag{11}$$

with disintegration proceeding only if the rate exceeds 10^3 s^{-1}. Here β is the fragmentation channel degeneracy (taken to be n for small Ar_n-HCO^+ clusters), ν is a typical cluster vibrational frequency ($\nu/c \approx 50$ cm^{-1}), $D(n)$ is the dissociation energy for the nth Ar, and $s = 3n$ is the number of degrees of freedom.

Given a set of incremental binding energies $D(n)$ and IR excitation energies, branching ratios for fragments from a Ar_n-HCO^+ cluster are predicted in the following fashion. (1) The initial energy distribution is determined by shifting the thermal energy distribution (eq 10 with $\nu/c = 50$ cm^{-1}, $T = 35$ K) upwards by the photon energy. (2) If the clusters' internal energy exceeds the dissociation energy and if fragmentation is sufficiently rapid ($k > 10^3$ s^{-1}), evaporative loss of an Ar atom ensues, giving rise to fragment clusters whose internal energy distributions are predicted using eq 8. Clusters with internal energy less than the dissociation energy or with fragmentation rates less than 10^3 s^{-1} are deemed stable. (3) Step 2 is repeated for the daughter clusters and for daughters of daughters and so on. By keeping a note of the fraction of stable clusters at each fragmentation stage, the branching ratios for production of fragment clusters containing $n - 1$, $n - 2$, $n - 3$, etc. Ar atoms are predicted. In the modified low kinetic energy release approach, the first Ar was assumed to depart with close to zero kinetic energy while further evaporations were governed by the procedure outlined above.

Eventually, the incremental binding energies using both approaches were determined in a least-squares fashion, being adjusted using the downhill simplex method[41] to minimize the squared difference between observed and calculated photofragmentation branching ratios for both ν_1 and $\nu_1 + \nu_s$ bands of the entire Ar_n-HCO^+ ($n = 1-13$) series. To begin the optimization procedure it is necessary to supply a set of estimated binding energies. Experience showed that the final binding energies could depend significantly on the initial estimated ones and that there was a tendency for the procedure to locate local rather than global minima. However, it was also observed that one set of final binding energies, which could be reached from widely varying initial conditions, produced a much better match between the calculated and observed branching ratios. The optimized binding energies $D(n)$ and corresponding branching ratios obtained through both approaches are summarized respectively in Tables 3 and 4. Generally, it was found that the agreement between modeled and measured branching ratios was greatly improved for the low kinetic energy release scheme. Thus, the sum of the squared differences between the measured and calculated branching ratios was 0.37 for the unmodified approach and 0.025 for the modification (zero translational kinetic energy for the first Ar lost).

The general pattern for both treatments is that incremental binding energies drop at particular n values ($n = 5$ and $n = 12$ for both approaches as well as $n = 1$ for the modified approach) and then plateau or grow slightly with increasing n (see Table 3 and Figure 6c). Perhaps the largest difference is that the modified version predicts a significantly larger binding energy for the first Ar atom (1200 cm^{-1} against 910 cm^{-1}). As expected, the effect of setting the first fragment's kinetic energy to zero is most significant for the smaller clusters, with the unmodified Engelking approach giving clearly lower binding energies ($D_{av} = 865$ cm^{-1} for $n = 2-5$) compared to the low kinetic energy release version ($D_{av} = 978$ cm^{-1} for $n = 2-5$). For clusters larger than Ar_5-HCO^+ ($n = 6-12$) predictions

for both approaches are closer: $D_{av} = 663$ cm^{-1} for the unmodified version and $D_{av} = 702$ cm^{-1} for the low kinetic energy release model.

Although it is not immediately obvious which of the two decomposition schemes is more appropriate, it is certainly the case that the reduced kinetic energy scheme produces much better agreement with the branching ratio data and yields a more physically likely series of binding energies for the smaller clusters; it seems improbable that the binding energies for the second, third, and fourth Ar atoms would be as high as for the first. Surprisingly, the binding energies extracted from the branching ratios agree quite well with the ones determined in the structure calculations described in section IVa (see Figure 6c). The obvious discrepancy is for Ar_6–HCO^+. While both treatments of the branching ratio data predict a drop from $n = 5$ to $n = 6$, the structure calculation binding energies show a decrease between $n = 6$ and $n = 7$.

In order to evaluate the dissociation and energy partitioning schemes employed here, it may be useful in future to compare the Ar binding energies with data obtained using other methods (e.g., high-pressure mass spectrometry,[57] or fitting of fragment kinetic energy release data[58] or metastable fractions[59] to evaporative ensemble models). Hopefully, for the Ar–HCO^+ dimer a relatively accurate estimate for the dissociation energy will soon be available from potentials based upon spectroscopic data.

V. Discussion and Summary

Generally, one may expect that the most stable Ar_n–HCO^+ cluster structures will be ones which maximize coordination between the Ar atoms and the most positively charged part of the HCO^+ core (and to a lesser extent with one another). The mid-infrared spectra strongly suggest that this is indeed the case with Ar atoms preferentially adopting positions close to the hydrogen and carbon atoms, which according to the Mulliken population analysis[42] should carry most positive charge. The first Ar atom occupies a linear proton-bound position with further argons sited in primary ($n = 2$–5) and secondary ($n = 5$–11) solvation rings. An alternative Ar_{12}–HCO^+ structure proposed by Stace, whereby the oxygen atom is immersed within a shell of Ar atoms, with the positively charged carbon and hydrogen atoms dangling loose,[60] seems to be less probable.

One apparent anomaly concerns the filling of the first solvation ring. While the calculations detailed in section IVa suggest that this should occur at $n = 6$, most of the cluster properties (including the binding energies derived from the branching ratios, band shifts, line widths, and combination band spacings) exhibit a noticeable discontinuity on going from $n = 5$ to $n = 6$ (Figure 6). This strongly suggests that while up to six ligands can comfortably coordinate with the proton (one CO molecule, five Ar atoms: one linearly disposed, four arranged in a ring), the introduction of an additional Ar into the first solvation ring occasions some degree of strain. Thus, formation of a second ring may already begin at Ar_6–HCO^+, with completion of the first ring occurring at a later stage. It is also feasible that two or more energetically close lying isomers exist for Ar_n–HCO^+ ($6 \leq n \leq 10$), one with four Ar atoms in the first ring, the other with five. In this regard, it is perhaps significant to note that the ν_1 band for clusters in this range features a subsidiary peak, lying a few wavenumbers to higher energy from the main one, which may be associated with a less stable isomer (Figure 5). Enthalpies for the $N_2 + H(N_2)_{n-1}^+ \leftrightarrow H(N_2)_n^+$ and $CO + H(CO)_{n-1}^+ \leftrightarrow H(CO)_n^+$ clustering reactions exhibit pronounced drops at the corresponding point (between $n = 6$ and $n = 7$), an observation that has also been linked to the formation of an octahedral coordination shell about a central proton for $n = 6$.[61]

The plot of binding energy against cluster size (Figure 6c) is to some extent reminiscent of the abundance data for Ar_n–HCO^+ clusters formed through electron impact ionization of neutral argon/dimethyl ether clusters.[60] Most noticeable is a pronounced drop in both binding energies and the cluster abundances on going from $n = 12$ to 13, probably corresponding to the completion of the first icosahedral shell and beginning of the second. The Ar_n–HCO^+ abundance also falls sharply between $n = 6$ and $n = 7$, a decrease that is not matched in the binding energies extracted from the branching ratios. Unfortunately, the mass spectral data do not extend below Ar_6–HCO^+, making it impossible to see whether a drop in the abundance also occurs between $n = 5$ and $n = 6$.[60] Mass spectra of clusters produced by our source do not exhibit prominent magic numbers, possibly due to the fact that clusters are formed through a relatively gentle process of coalescence rather than through neutral cluster ionization, followed by internal ion molecule reactions and evaporative ligand loss.

The significant points emerging from the current work can be summarized as follows:

1. The Ar–HCO^+ dimer appears to possess a linear proton-bound equilibrium structure. Assuming an undistorted HCO^+ monomer, the complexes' rotational constants are consistent with a proton–argon separation of 2.13 Å in the ground state and 2.08 Å in the ν_1 state. The huge ν_1 vibrational red shift of 274 cm^{-1} emphasizes the relatively strong interaction between the proton and the Ar atom. Upper limits of approximately 2×10^{-7} cm^{-1} for the D values suggest that the intermolecular stretch vibration has a frequency of at least 70 cm^{-1}, consistent with the assignment of a weak band situated 146 cm^{-1} above ν_1 as the $\nu_1 + \nu_s$ combination band.

2. For the larger clusters, the development of several cluster properties with size including the incremental binding energies, vibrational red shifts, and ν_1 line widths is argued to be consistent with cluster structures whereby the first and most strongly bound Ar atom is added in a linear proton-bound configuration with subsequent Ar atoms forming first primary and then secondary solvation rings each containing four or five Ar atoms. A distinct drop in the binding energy for $n = 13$ and also the appearance of an additional ν_1 peak can be convincingly associated with the beginning of a second solvation shell about an Ar_{12}–HCO^+ icosahedral core.

There are several obvious avenues for further work. In the first place, a more complete understanding of the Ar···HCO^+ interaction potential would be desirable, especially in regions away from the minimum. A better potential would not only help to fully characterize the close range interaction between the Ar atom and HCO^+ molecular ion but would also lay the foundation for a better understanding of the spectroscopic and dynamical behavior of the larger cluster species. To this end the measurement and analysis of combination bands involving the intermolecular vibrations in Ar–HCO^+ are crucial.

Acknowledgment. E.J.B. is pleased to acknowledge discussions with Prof. R. O. Watts concerning vibrational band shifts in clusters. The innovative contributions of Mr. K. Mutschler to equipment development are appreciated. Support for this work under the BBW grant No. 93.02060 is acknowledged. This work is part of project No. 20-41768.94 of Schweizerischer Nationalfonds zur Förderung der wissenschaftlichen Forschung.

References and Notes

(1) *Cluster Ions*; Ng, C.-Y., Baer, T., Powis, I., Eds.; Wiley: Chichester, U.K., 1993.

(2) *Clusters of Atoms and Molecules*; Haberland, H., Ed.; Springer-Verlag: Berlin, 1994; Vol. 56.
(3) Harris, I. A.; Kidwell, R. S.; Northby, J. A. *Phys. Rev. Lett.* **1984**, *53*, 2390.
(4) Arnold, S. T.; Hendricks, J. H.; Bowen, K. H. *J. Chem. Phys.* **1995**, *102*, 39.
(5) Mackay, A. L. *Acta. Crystallogr.* **1962**, *15*, 916.
(6) Gutowsky, H. S.; Chuang, C.; Klots, T. D.; Emilsson, T.; Ruoff, R. S.; Krause, K. R. *J. Chem. Phys.* **1988**, *88*, 2919.
(7) Elrod, M. J.; Saykally, R. J. *Chem. Rev.* **1994**, *94*, 1975.
(8) Nesbitt, D. J. *Annu. Rev. Phys. Chem.* **1994**, *45*, 367.
(9) Buck, U.; Huisken, F.; Lauenstein, C.; Meyer, H.; Sronka, R. *J. Chem. Phys.* **1987**, *87*, 6276.
(10) Buck, U. *J. Phys. Chem.* **1988**, *92*, 447.
(11) Huisken, F. *Adv. Chem. Phys.* **1992**, *81*, 63.
(12) Lisy, J. M. In *Cluster Ions*; Ng, C.-Y., Baer, T., Powis, I., Eds.; Wiley: Chichester, U.K., 1993.
(13) Okumura, M.; Yeh, L. I.; Lee, Y. T. *J. Chem. Phys.* **1988**, *88*, 79.
(14) Okumura, M.; Yeh, L. I.; Myers, J. D.; Lee, Y. T. *J. Phys. Chem.* **1990**, *94*, 3416.
(15) Price, J. M.; Crofton, M. W.; Lee, Y. T. *J. Phys. Chem.* **1991**, *95*, 2182.
(16) Price, J. M.; Crofton, M. W.; Lee, Y. T. *J. Chem. Phys.* **1989**, *91*, 2749.
(17) Lias, S. G.; Bartmess, J. E.; Liebman, J. F.; Holmes, J. L.; Levin, R. D.; Mallard, W. G. *J. Phys. Chem. Ref. Data* **1988**, *17*,
(18) Engelking, P. C. *J. Chem. Phys.* **1986**, *85*, 3103.
(19) Engelking, P. C. *J. Chem. Phys.* **1987**, *87*, 936.
(20) Nizkorodov, S. A.; Maier, J. P.; Bieske, E. J. *J. Chem. Phys.* **1995**, *103*, 1297.
(21) Nizkorodov, S. A.; Maier, J. P.; Bieske, E. J. *J. Chem. Phys.* **1995**, *102*, 5570.
(22) Bieske, E. J.; Nizkorodov, S. A.; Bennett, F. R.; Maier, J. P. *J. Chem. Phys.* **1995**, *102*, 5152.
(23) Bieske, E. J.; Nizkorodov, S. A.; Bennett, F. R.; Maier, J. P. *Int. J. Mass Spectrom. Ion Processes*, in press.
(24) Daly, N. R. *Rev. Sci. Instrum.* **1960**, *31*, 264.
(25) Bieske, E. J. *Faraday Trans.* **1995**, *91*, 1.
(26) Guelachvili, G.; Rao, K. N. *Handbook of Infrared Standards*; Academic Press Inc.: London, 1993; Vol. 2.
(27) Millen, D. C. *Can. J. Chem.* **1985**, *63*, 1477.
(28) Sastry, K. V. L. N.; Herbst, E.; DeLucia, F. C. *J. Chem. Phys.* **1981**, *75*, 4169.
(29) Drucker, S.; Cooksy, A. L.; Klemperer, W. *J. Chem. Phys.* **1993**, *98*, 5158.
(30) Leopold, K. R.; Fraser, G. T.; Lin, F. J.; Nelson, D. D.; Klemperer, W. *J. Chem. Phys.* **1984**, *81*, 4922.
(31) Fraser, G. T.; Pine, A. S. *J. Chem. Phys.* **1989**, *91*, 3319.
(32) Liu, S.-y.; Dykstra, C. E. *J. Phys. Chem.* **1986**, *90*, 3097.
(33) Nizkorodov, S. A.; Maier, J. P.; Bieske, E. J., unpublished results.
(34) Jortner, J.; Even, U.; Leutwyler, S. *J. Chem. Phys.* **1983**, *78*, 309.
(35) Asher, R. L.; Micha, D. A.; Brucat, P. J. *J. Chem. Phys.* **1992**, *96*, 7683.
(36) Woods, R. C. *Philos. Trans. R. Soc. A* **1988**, *324*, 141.
(37) Hutson, J. *Annu. Rev. Chem. Phys.* **1990**, *41*, 123.
(38) Brocks, G.; Huygen, T. *J. Chem. Phys.* **1986**, *85*, 3411.
(39) Nemethy, G.; Pottle, M. S.; Scheraga, H. A. *J. Phys. Chem.* **1983**, *87*, 1883.
(40) *Molecular Structure and Properties*; Buckingham, A. D., Ed.; Butterworth: London, 1975; Vol. 2.
(41) Nelder, J. A.; Mead, R. *Comput. J.* **1965**, *7*, 308.
(42) Weis, B.; Yamashita, K. *J. Chem. Phys.* **1993**, *99*, 9512.
(43) Stone, A. J. *Chem. Phys. Lett.* **1981**, *83*, 233.
(44) Gudeman, C. S.; Begemann, M. H.; Pfaff, J.; Saykally, R. J. *Phys. Rev. Lett.* **1983**, *50*, 727.
(45) Levy, D. H. *Adv. Chem. Phys.* **1981**, *47*, 323.
(46) Gutowsky, H. S.; Klots, T. D.; Chuang, C.; Keen, J. D.; Schuttenmaer, C. A.; Emilsson, T. *J. Am. Chem. Soc.* **1987**, *109*, 5633.
(47) Gutowsky, H. S.; Klots, T. D.; Chuang, C.; Schuttenmaer, C. A.; Emilsson, T. *J. Chem. Phys.* **1987**, *86*, 569.
(48) Gutowsky, H. S.; Klots, T. D.; Chuang, C.; Keen, J. D.; Schuttenmaer, C. A.; Emilsson, T. *J. Am. Chem. Soc.* **1985**, *107*, 7174.
(49) McIlroy, A.; Lascola, R.; Lovejoy, C. M.; Nesbitt, D. J. *J. Phys. Chem.* **1991**, *95*, 2636.
(50) McIlroy, A.; Nesbitt, D. J. *J. Chem. Phys.* **1992**, *97*, 6044.
(51) Liu, S.; Bacic, Z.; Moskowitz, J. W.; Schmidt, K. E. *J. Chem. Phys.* **1994**, *101*, 10181.
(52) Bieske, E. J.; Soliva, A. M.; Friedmann, A.; Maier, J. P. *J. Chem. Phys.* **1992**, *96*, 28.
(53) Friedmann, A.; Soliva, A. M.; Nizkorodov, S. A.; Bieske, E. J.; Maier, J. P. *J. Phys. Chem.* **1994**, *98*, 8896.
(54) Liu, D.-J.; Lee, S.-T.; Oka, T. *J. Mol. Spectrosc.* **1988**, *128*, 236.
(55) Foster, S. C.; McKellar, A. R. W. *J. Chem. Phys.* **1984**, *81*, 3424.
(56) Ewing, G. E. *J. Phys. Chem.* **1987**, *91*, 4662.
(57) Keesee, R. G.; Castleman, Jr., A. W. *J. Phys. Chem. Ref. Data* **1986**, *15*, 1011.
(58) Lifschitz, C. In *Cluster Ions*; Ng, C.-Y., Baer, T., Powis, I., Eds.; Wiley: Chichester, U.K., 1993.
(59) Wei, S.; Tzeng, W. B.; Castleman, A. W. *J. Chem. Phys.* **1990**, *93*, 2506.
(60) Stace, A. J. *J. Am. Chem. Soc.* **1984**, *106*, 4380.
(61) Hiraoka, K.; Saluja, P. P.; Kebarle, P. *Can. J. Chem.* **1979**, *57*, 2159.

JP951954S